Monthly Notices of the ROYAL ASTRONOMICAL SOCIETY

MNRAS **518,** 5106–5122 (2023) https://doi.org/10.1093/mnras/stac3382
Advance Access publication 2022 November 23

Spectral classification of the 100 pc white dwarf population from *Gaia*-DR3 and the virtual observatory

F. M. Jiménez-Esteban,[1]★ S. Torres,[2,3] A. Rebassa-Mansergas,[2,3] P. Cruz ,[1] R. Murillo-Ojeda,[1] E. Solano,[1] C. Rodrigo[1] and M. E. Camisassa[4]

[1]*Centro de Astrobiología (CAB), CSIC-INTA, Camino Bajo del Castillo s/n, Campus ESAC, E-28692 Villanueva de la Cañada, Madrid, Spain*
[2]*Departament de Física, Universitat Politècnica de Catalunya, c/Esteve Terrades 5, E-08860 Castelldefels, Spain*
[3]*Institut d'Estudis Espacials de Catalunya, Ed. Nexus-201, c/Gran Capità 2-4, E-08034 Barcelona, Spain*
[4]*Department of Applied Mathematics, University of Colorado, Boulder, CO 80309-0526, USA*

Accepted 2022 November 10. Received 2022 November 4; in original form 2022 September 16

ABSTRACT

The third data release of *Gaia* has provided low-resolution spectra for ∼100 000 white dwarfs (WDs) that, together with the excellent photometry and astrometry, represent an unrivalled benchmark for the study of this population. In this work, we first built a highly complete volume-limited sample consisting in 12 718 WDs within 100 pc from the Sun. The use of Virtual Observatory Spectral energy distribution Analyzer tool allowed us to perform an automated fitting of their spectral energy distributions to different atmospheric models. In particular, the use of spectrally derived *Javalambre-Physics of the Accelerating Universe Astrophysical Survey* photometry from *Gaia* spectra led to the classification of DA and non-DA WDs with an accuracy >90 per cent, tested in already spectroscopically labelled objects. The excellent performance achieved was extended to practically the whole population of WDs with effective temperatures above 5500 K. Our results show that while the A branch of the *Gaia* WD Hertzsprung–Russell diagram is practically populated by DA WDs, the B branch is largely formed by non-DAs (65 per cent). The remaining 35 per cent of DAs within the B branch implies a second peak at ∼0.8 $M_{\odot}$ in the DA mass distribution. Additionally, the Q branch and its extension to lower temperatures can be observed for both DA and non-DA objects due to core crystallization. Finally, we derived a detailed spectral evolution function, which confirms a slow increase of the fraction of non-DAs as the effective temperature decreases down to 10 500 K, where it reaches a maximum of 36 per cent and then decreases for lower temperatures down to ∼31 per cent.

Key words: astronomical data bases: miscellaneous – catalogues – Galaxy: stellar content – stars: evolution – *(stars:)* white dwarfs – virtual observatory tools.

1 INTRODUCTION

The excellent quality of astrometric and photometric data provided by the European Space Agency mission *Gaia* has been recently improved by the publication in its third data release (DR3) of nearly 200 million spectra (De Angeli et al. 2022). These spectra, although having a very low resolution ($R \approx 60$), represent an invaluable source of information for a wide range of stellar objects in our Galaxy. In particular, nearly 100 000 spectra correspond to white dwarfs (WDs; Gaia Collaboration 2022a).

As it is well known, WDs are stellar remnants of low- to intermediate-mass main-sequence stars (Althaus et al. 2010). Since nuclear fusion processes have ceased after the earlier stages of their lives, WDs are stellar objects supported against gravity by Fermi electron pressure and they are doomed to a long-standing cooling process. As this physical process is relatively well understood and some WDs can reach very old ages (10 Gyr or older), they can be used as reliable cosmochronometers (Fontaine, Brassard & Bergeron 2001), revealing valuable information about the history and evolution of our Galaxy (García-Berro & Oswalt 2016).

The source of energy in the deep interior of WDs – basically due to the gravothermal energy released by the ions and eventually provided by core crystallization, phase separation, and sedimentation of minor species among other processes (see Isern, Torres & Rebassa-Mansergas 2022, for a recent review) – is controlled by a thin partially degenerate layer through which the heat is radiated away. In the canonical model, this layer is formed by helium with a mass around 10^{-2} $M_{\odot}$, representing <2 per cent of the total WD mass, and in most of the cases (∼80 per cent), an extra thinner layer of hydrogen with a mass between 10^{-15} and 10^{-4} $M_{\odot}$ that lies on top of the helium one.

Observationally, characterization of WDs has been carried out mainly from spectroscopy, based on the atmospheric observed features, e.g. through the identification of Balmer and helium lines, among others (Sion et al. 1983). If the WD spectrum presents hydrogen lines, the WD is labelled as DA; however, if the spectrum presents absorption helium lines, He I or He II, the WD is named DB or DO, respectively. Although less common, it is possible to identify some metals within WD atmospheres, such as carbon, named

★ E-mail: fran.jimenez-esteban@cab.inta-csic.es

DQ, or other heavy elements such as Ca II or Fe II, assigned to the DZ spectral type. Some WDs can also present featureless spectra, named in this case as DC. This last condition is usually satisfied by cool objects, in particular for hydrogen-dominated atmospheres with effective temperatures ($T_{\rm eff}$) below ∼5000 K, or for helium-dominated atmospheres with $T_{\rm eff} \lesssim 11\,000$ K. This initial list of spectral types has been extended to include mixed cases. Thus, we can find hydrogen-dominated atmospheres with some helium features, named DAB, or the contrary case, DBA, or any possible combination such as DBQ, DAZ, and so on. Also possible is the detection of a magnetic field or the existence of some variability in the WD spectrum, adding in these cases and extra H or V, respectively, to the basic spectral type, e.g. DAH, DAV, and DQV. All in all, we can summarize the spectral classification of the WD population in two main classes: those with a hydrogen-dominated atmosphere (which is by far the most common case), DA, and the rest, named as non-DA. In any case, the importance of determining the atmospheric content of a WD is crucial, not only for understanding the physical processes in their evolution, but also to derive reliable individual parameters such as masses, temperatures, and ages.

Spectral identification has historically relied on visual inspection of spectra. However, with the advent of large spectroscopic surveys, such as Sloan Digital Sky Survey (SDSS; York et al. 2000), *Large Sky Area Multi-Object Fibre Spectroscopic Telescope* (Zhao et al. 2012), *Gaia* (Gaia Collaboration 2016), and many others, new automated data analysis techniques are required. In this sense, the Spanish Virtual Observatory (SVO) developed a powerful tool, the *Virtual Observatory Spectral energy distribution Analyzer* (VOSA[1]; Bayo et al. 2008). VOSA is a Virtual Observatory (VO) tool that allows the user to build spectral energy distributions (SEDs) from both private and public photometric data within the VO, of thousands of objects at a time, and to derive their physical properties by comparing the observed SEDs to different collections of theoretical models. Moreover, it can estimate the goodness of the fitting of the model to the observed data.

In this work, we aimed at thoroughly analysing the 100 pc nearly complete volume-limited sample of WDs with the main objective of individually classifying them based on their main spectral type class (DA or non-DA). The paper is, thus, organized as follows. After this introduction, in Section 2, we describe our methodology for building our volume-complete observed sample of WDs within 100 pc from the Sun. In Section 3, we detail the different WD atmospheric models used, and how the SEDs were built from VO photometry or from synthetic photometry derived from the *Gaia* spectra. In Section 4, we introduce a set of WD spectral type estimators based on the VOSA fitting and also, for comparative purposes, others estimators based on data found in the literature. In Section 5, we apply the best estimator found on the basis of an already classified population of WDs to the entire population, thus obtaining reliable distributions of stellar parameters, such as mass and effective temperature. Finally, we summarize our main results and conclusions in the last section.

2 THE *GAIA*-DR3 100 PC WD SAMPLE

In this section, we describe our methodology for identifying WD candidates within 100 pc in the *Gaia*-DR3 catalogue.

In Jiménez-Esteban et al. (2018, hereafter JE18), we demonstrated that the completeness of the 100 pc WD sample selected using the second *Gaia* data release (DR2; Gaia Collaboration 2018) reached

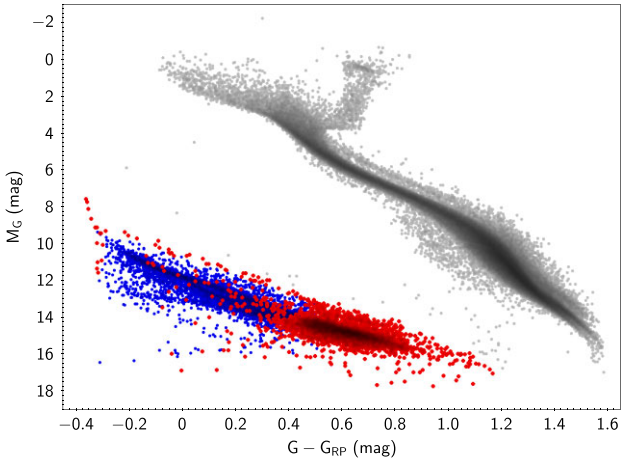

Figure 1. *Gaia* HR diagram of all *Gaia* sources within 100 pc considered in this work. WDs already identified in the *Gaia*-DR2 catalogue by JE18 are plotted in blue, and in red the new candidates identified in the *Gaia*-DR3 catalogue. Those stars fulfilling our 100 pc selection criteria but not selected as WD candidates are shown in grey.

∼94 per cent for a parallax relative error lower than ∼10 per cent. We also noted that smaller samples in volume are not necessarily more complete due to the Lutz–Kelker bias (Lutz & Kelker 1973) and that for larger volumes, the completeness also decreases due to the magnitude limit of the *Gaia* satellite (Gaia Collaboration 2016). As a consequence, we focused in this work on the construction of a WD catalogue up to 100 pc by selecting *Gaia*-DR3 sources with parallaxes larger than 10 mas, considering the errors, and imposing relative errors smaller than 10 per cent in parallax and in *BP*- and *RP*-band photometry. Photometric errors in the *BP* and *RP* bands were especially important for faint sources in crowded areas. Since the *G*-band photometry had lower error than the other two bands, we did not impose any cut in the *G* band. Thus, we queried the *Gaia*-DR3 catalogue[2] using the following criteria:

(i) $\omega - 3\sigma_\omega \geq 10$ mas and $\omega/\sigma_\omega \geq 10$;
(ii) $F_{\rm BP}/\sigma_{F_{\rm BP}} \geq 10$ and $F_{\rm RP}/\sigma_{F_{\rm RP}} \geq 10$; and
(iii) Renormalized Unit Weight Error (RUWE) < 1.4.

The cut in the *RUWE* parameter prevented against poor astrometric solutions (Lindegren et al. 2021). These criteria guaranteed that the sources were indeed within the 100 pc volume. In addition, we estimated the corrected *BP* and RP flux excess factor (C^*) and its scatter (σ_{C^*}), and applied a $3\sigma_{C^*}$ cut following the recommendations by Riello et al. (2021). This criterion excluded some objects in the coolest end of the WD sequence, where the oldest WDs are expected. However, this guaranteed the consistency between the *G*-band photometry and the *BP* and RP photometry.

We show in Fig. 1, the *Gaia* Hertzsprung–Russell (HR) diagram for all sources within 100 pc with good photometric and astrometric data, as defined by the above criteria. Since the *BP*-band photometry has a known bias for red and faint sources (Fabricius et al. 2021), we used the $G - G_{\rm RP}$ colour instead of the more commonly adopted $G_{\rm BP} - G_{\rm RP}$. The 10 per cent of uncertainty of the *Gaia* fluxes corresponds to an uncertainty of ∼0.14 mag in the *Gaia* colour. On the other hand, the 10 per cent uncertainty in the parallax corresponds to an uncertainty of ∼0.2 mag in the absolute *G*-band magnitude. This

[1] http://svo2.cab.inta-csic.es/theory/vosa

[2] http://gea.esac.esa.int/archive/

Table 1. Available SIMBAD classification for 12 454 of our selected *Gaia*-DR3 WDs. Classifications in agreement with the WD nature of our selected candidates are listed above and shown in italics. The estimated contamination is ≲0.1 per cent.

SIMBAD class	*N* (candidates)
WD	3640 (7242)
Blue object	4
Star	80
High proper motion	1449
In binary/multiple system	18
Hot subdwarfs	12 (2)
Cataclysmic variable	4 (1)
Variable star	1
Emission-line star	1

diagram clearly shows the *main sequence*, the *red giant branch*, and the *WD sequence*. Based on the location within the colour–magnitude diagram, we selected 12 718 *Gaia*-DR3 sources located in the *WD Sequence* (blue and red dots in Fig. 1), thus representing our 100 pc sample. It is worth noting that 7480 of these sources (blue) were already in the *Gaia*-DR2 WD catalogue[3] by JE18, and that 5238 (red) are new incorporations from the *Gaia*-DR3 catalogue.

The *Gaia*-DR2 WDs are located in Fig. 1 at bluer colour ($G - G_{RP} \lesssim 0.5$ mag); however, most of the newly identified have redder colours up to $G - G_{RP} \sim 1.2$ mag. This is because JE18 imposed a colour limit of $G_{BP} - G_{RP} < 0.8$ mag, corresponding to a T_{eff} of ∼6000 K, to avoid contamination by field stars with bad *Gaia*-DR2 astrometry. Thanks to the improvement in the astrometry measurements of the *Gaia*-DR3, this colour cut is no longer needed, allowing us to study the red part of the *WD sequence*. There is also a number of hotter WDs ($G_{BP} - G_{RP} < 0.8$ mag) that were not included in the *Gaia*-DR2 WD catalogue by JE18. Fifty one of them are located in the HR diagram above the box defined in that work. The rest was not included probably due to lower quality of the *Gaia*-DR2 astrometry and/or photometry. On the other hand, there are 139 WD candidates within 100 pc identified by JE18 from the *Gaia*-DR2 catalogue which are now excluded from the new catalogue using *Gaia*-DR3. This is probably due to a wrong astrometric solution in the *Gaia*-DR2 catalogue.

In conclusion, the catalogue of WDs within 100 pc presented in this work, not only extends to redder colours than the previous one, but also discards misidentified objects and includes blue missing sources. This catalogue, containing the basic information of the selected sources, including the spectral classification (Section 4) and the physical parameters (Section 5.2) derived in this work, can be accessed electronically through our online catalogue service (see Appendix A).

2.1 Contamination

We used the SIMBAD data base to evaluate the contamination in our WD catalogue by other types of sources. We searched for SIMBAD counterparts within 3 arcsec of our *Gaia* WD candidates using the *Gaia*-DR3 coordinates translated to epoch J2000 and corrected from *Gaia*-DR3 proper motions. Approximately 98 per cent (12 454) of the sample had a counterpart in SIMBAD, all of them with a classification, at least tentative. The results are shown in Table 1.

[3]http://svo2.cab.inta-csic.es/vocats/v2/wdw/

If we assume the SIMBAD classifications to be correct, including those flagged as candidates, and taken into account the position of these sources in the *Gaia* colour–magnitude diagram (see Fig. 1), one can conclude that most (>99.8 per cent) of them have classifications compatible with WD nature.

The highest source of contamination seems to be hot subdwarfs (∼0.1 per cent) and cataclysmic variables (∼0.04 per cent). However, although hot subdwarfs have similar colours than hot WDs, they are more luminous and should occupy a different region in the HR diagram. So, the classification provided by SIMBAD is likely to be incorrect, and these objects are most probably misclassified WDs. Thus, the expected contamination in our WD catalogue is very low (<0.1 per cent).

2.2 Completeness

Our 100 pc WD sample is volume-limited and has a very low degree of contamination sample. However, it is subject to the astrometric and photometric constrains that were imposed to the *Gaia*-DR3 catalogue as explained above. Recently, from the *Gaia*-DR2 catalogue, Hollands et al. (2018) estimated a space-density of 4.49×10^{-3} pc^{-3} for the WD population within 20 pc from the Sun. Assuming the same space-density up to 100 pc, we would expect ∼18.800 WD in this volume. This implies that the completeness of our sample is ∼70 per cent of the entire 100 pc WD population. This estimation is in agreement with Torres et al. (2022).

Nevertheless, the level of completeness is not homogeneous along the *Gaia* colour range presented by the sample. Fig. 5 of JE18 shows the completeness as a function of the $G_{BP} - G_{RP}$ colour of a similar sample within 100 pc obtained from the previous *Gaia*-DR2 catalogue. The completeness is almost 100 per cent for $G_{BP} - G_{RP} <$ 0 mag and it continuously decreases to ∼70 per cent for the reddest colours $G_{BP} - G_{RP} = 0.8$ mag. It is expected that the completeness continues decreasing for redder colours than $G_{BP} - G_{RP} = 0.8$ mag.

Our sample was built from the *Gaia*-DR3 catalogue, which has both better astrometry and photometry than the previous *Gaia*-DR2, so the completeness of the present sample is expected to be higher than the previous one. Consequently, we conclude that most of the missing sources are at the reddest colours, and the completeness of the spectroscopically classified sources ($G_{BP} - G_{RP} < 0.86$ mag; see Section 4) is larger than 90 per cent.

Regarding the missing objects, one cause of missing sources is the confusion in the Galactic plane. Using our WD sample, we compared the number of WDs per square degree in the Galactic plane ($|b| <$ 10 deg) and out of it. We found that the WD sky density in the Galactic plane is 5 per cent lower than in the rest of the sky. Thus, we estimated ∼120 missing WDs due to confusion. This is ∼1 per cent of our sample.

Another cause of missing WDs is the number of double degenerate systems (DWD) which were not resolved by *Gaia* and were counted as single WDs. Torres et al. (2022) used different models to estimate the fraction of such systems. The best model estimated a fraction between 1 and 3 per cent (depending on the common-envelope treatment) of unresolved DWDs within 100 pc.

Finally, the third cause of missing sources are the binary systems made up by a WD and a main-sequence AFGK star, also known as Sirius-like systems. Holberg et al. (2013) estimated that 8 per cent of the WDs in the solar vicinity are members of such systems. Since many of them are now resolved by *Gaia*, we can use this value as an upper limit of the missing WDs in our sample.

Summing up the contribution of missing sources, we conclude that <10 per cent of WDs located within 100 pc are not part of our

catalogue in the colour range $G_{BP} - G_{RP} < 0.86$ mag; however, in the reddest end of the WD sequence completeness decreases and the missing source would be mainly due to the limitations of *Gaia* capabilities in both astrometry and photometry.

3 SED ANALYSIS

In this section, we present the analysis of the SEDs of our 100 pc WD sample built from public photometric data and from *Gaia* spectra. Our purpose was to classify them in two main spectral classes: DA and non-DA. To that end, we used two different grids of WD atmosphere models: hydrogen-dominated atmospheres (type DA) and helium-dominated atmospheres (note that even though DB models were used, others spectral types were also expected and we therefore named this group as type non-DA). We did not account for interstellar extinction since our sample is located at short distances.

3.1 WD atmospheric models

The collection of models used in the analysis adopt local thermodynamic equilibrium, hydrostatic equilibrium, plane-parallel, one-dimensional structure, and convection with the mixing-length approximation where appropriate. The DA models consider pure hydrogen composition, and the non-DA models consider helium with a small trace of hydrogen ($\log N(H)/N(He) = -6$). The version of the mixing length is ML2 (Tassoul, Fontaine & Winget 1990), with the ratio of mixing-length to pressure scale height 0.7 in the DA and 1.25 in the non-DA WDs. Basic methods and data are described in Koester (2010). More recently many improvements were implemented, the most important being, namely, improved treatment of molecules, non-ideal effects, and unified line broadening theories for the strong lines of Mg I, Mg II, Ca I, Ca II, and Ly α. Also, the hydrogen Stark profiles by Tremblay & Bergeron (2009) and Tremblay (private communication) are included.

The DA grid contains 1260 model spectra and covers effective temperatures from 3000 to 20 000 K in steps of 250 K (note that below ∼5000 K these WDs are DCs), from 20 000 to 30 000 K in steps of 1000 K, and from 30 000 to 40 000 K in steps of 2000 K. For each effective temperature, the surface gravities range from 6 to 9.25 dex in steps of 0.25 dex. The non-DA grid contains 666 model spectra and, in this case, the effective temperatures cover the 5500–20 000 K range in steps of 250 K (below ∼10 000 K these WDs are also featureless DCs), the 20 000–30 000 K range in steps of 1000 K, and the range from 30 000–40 000 K in steps of 2000 K. For this grid, the surface gravities range from 7 to 9 dex in steps of 0.25 dex for each effective temperature value.

3.2 SED from VO archives

To build the SEDs of the 100 pc WD sample from public archives within the VO, we collected data from different photometric catalogues, which are listed in Table 2. Detailed information of the adopted filters can be found using the SVO Filter Profile Service[4] (Rodrigo, Solano & Bayo 2012; Rodrigo & Solano 2020). In order to avoid misidentifications, the *Gaia* coordinates for all sources were corrected from proper motion and transformed to an epoch closer to the observation epoch for each of the queried survey. A 3 arcsec search radius was adopted. This allowed us to build the observational SEDs from the ultraviolet (UV) to the mid-infrared (mid-IR) wavelength range for most of the sources.

For 463 WD candidates, no additional photometry to *Gaia* data were found, so their SEDs could not be fitted with VOSA. For the other 12 255 sources, each individual SED was fitted to both DA and non-DA WD synthetic spectra outlined in Section 3.1. Of them, we obtained a reliable fit, defined as $\mathrm{Vgf}_b < 15$,[5] for 10 447 sources when using either DA or non-DA model spectra. When using DA model spectra, 1104 WDs obtained good fits only; however, 65 WDs obtained good fits only when using non-DA model spectra. In total, we obtained a good fit for 11 616 sources (∼95 per cent of the fitted sample).

For illustrative purposes, in the left-hand panels of Fig. 2, we show the observational SEDs built from VO photometric catalogues (red circles), together with the synthetic photometry (blue squares) and the synthetic spectra (grey solid line) that best fit the observations. The two upper rows correspond to two WDs whose best-fit model is a DA, and the two bottom rows correspond to two WDs whose best-fit model is a non-DA, with different effective temperatures and surface gravities. In the right-hand panels of Fig. 2, we also show for the same sources, the SEDs built with the J-PAS photometry obtained from *Gaia* spectra (see Section 3.3).

3.3 SED from *Gaia* spectra

The new *Gaia*-DR3 has provided low-resolution spectra for more than 200 million sources (De Angeli et al. 2022). The spectra cover the optical to near-infrared (near-IR) wavelength range, from 330 to 1050 nm, approximately. A total of 12 342 (97 per cent of the whole ample) WDs in our sample had *Gaia* low-resolution spectra available. We used the Python package GAIAXPY[6] to construct the photometric SEDs of these sources from *Gaia* spectra using the J-PAS (Benitez et al. 2014) filter system (Marín-Franch et al. 2012). This system is composed of 54 overlapping narrow-band (full width at half-maximum ≈ 145 Å) filters covering from 3780 to 9100 Å, plus two broad-band filters at the blue and red end of the optical range, and four complementary SDSS-like filters. In total, the 60 J-PAS filters provide a low-resolution ($R \approx 60$) spectrum (Bonoli et al. 2021) similar to *Gaia*. However, due to the low signal-to-noise ratio of the *Gaia* spectra at bluer wavelengths (Gaia Collaboration 2022a), we did not use the four J-PAS filters with effective wavelength shorter than 4000 Å, which reduces to 56 the number of J-PAS filters available for building the SEDs. Detailed information on the J-PAS filter system can be found at the SVO Filter Profile Service.[7]

For each source in our sample with a *Gaia* spectrum, we built two SEDs using the J-PAS photometric system, one taking into account all the coefficients of the spectrum (GJP) and one taking into account only the relevant coefficients as provided by *Gaia*-DR3 (GJP-trunc) (De Angeli et al. 2022). We imposed a threshold in the photometric error of 10 per cent to each individual photometric measurement obtained with GAIAXPY. Thus, although most of the SEDs have 56 photometric points, in some noisy spectra the number of points is lower. For illustrative purposes, in Fig. 3 we show two SEDs built

[4]Available at: http://svo2.cab.inta-csic.es/theory/fps/.

[5]Vgf_b: Modified reduced χ^2, calculated by forcing $\sigma(F_{\mathrm{obs}})$ to be larger than $0.1 \times F_{\mathrm{obs}}$, where $\sigma(F_{\mathrm{obs}})$ is the error in the observed flux (F_{obs}). This can be useful if the photometric errors of any of the catalogues used to build the SED are underestimated. Vgf_b smaller than 10–15 is often perceived as a good fit.

[6]https://www.cosmos.esa.int/web/gaia/gaiaxpy

[7]http://svo2.cab.inta-csic.es/theory/fps/index.php?mode=browse&gname=OAJ&gname2=JPAS

Table 2. Photometry data from VO archives used to build the SEDs. The detailed information on each photometric filter can be obtained from the SVO Filter Profile Service (Rodrigo et al. 2012; Rodrigo & Solano 2020).

Survey	Facility/instrument	Spectral range	Filters	Reference
GALEX UV GR6+7	GALEX	UV	*FUN*, *NUV*	1
XMM-SUSS4.1	XMM/OM	UV, visible	*UVW2*, *UVM2*, *UVW1*, *U*, *B*, *V*	2
Gaia-DR3	Gaia	Visible	G_{BP}, G, G_{RP}	3
APASS DR9	–	Visible	*B*, *v*, *g*, *r*, *i*	4
J-PLUS DR1	OAJ/T80Cam	Visible	*uJAVA*, *J0378*, *J0395*, *J0410*, *J0430*, *gSDSS* *J0515*, *rSDSS*, *J0660*, *iSDSS*, *J0861*, *zSDSS*	5
Tycho-2	TYCHO	Visible	*B*, *V*	6
SDSS DR12	SLOAN	Visible	*u*, *g*, *r*, *i*, *z*	7
IPHAS DR2	INT/WFC	Visible	*gR*, *Ha*, *gI*	8
VPHAS+ DR2	Paranal/OmegaCAM	Visible	*u*, *g*, *H*α, *i*, *z*	9
Pan-STARRS1 DR2	PAN-STARRS	Visible, near-IR	*g*, *r*, *i*, *z*, *y*	10
Dark Energy Survey DR1	CTIO/DECam	Visible, near-IR	*g*, *r*, *i*, *z*, *Y*	11
DENIS	–	Visible, near-IR	*I*, *J*, K_s	12
VISTA	Paranal/VIRCAM	Visible, near-IR	*Z*, *Y*, *J*, *H*, K_s	13
UKIDSS	UKIRT/WFCAM	Visible, near-IR	*Z*, *Y*, *J*, *H*, *K*	14
2MASS	2MASS	Near-IR	*J*, *H*, K_s	15
GLIMPSE I+II+3D	Spitzer/IRAC	Mid-IR	*I1*, *I2*, *I3*, *I4*	16
AllWISE	WISE	Mid-IR	*W1*, *W2*, *W3*, *W4*	17

Note. References: [1] Revised catalog of GALEX UV sources (GALEX UV GR6+7; Bianchi, Shiao & Thilker 2017); [2] *XMM–Newton* Serendipitous Ultraviolet Source Survey catalogue (XMM-SUSS4.1; Page et al. 2012); [3] *Gaia*-DR3 (Gaia Collaboration 2022b); [4] AAVSO Photometric All-Sky Survey (APASS DR9; Henden et al. 2015); [5] Javalambre Photometric Local Universe Survey (J-PLUS DR1; Cenarro et al. 2019); [6] Tycho-2 Catalogue (Høg et al. 2000); [7] Sloan Digital Sky Survey Photometric Catalogue (SDSS DR12; Alam et al. 2015); [8] INT/WFC Photometric H-Alpha Survey of the Northern Galactic Plane Catalogue (IPHAS DR2; Barentsen et al. 2014); [9] VST Photometric Halpha Survey of the Southern Galactic Plane and Bulge (VPHAS+ DR2; Drew et al. 2016); [10] Panoramic Survey Telescope and Rapid Response System (Pan-STARRS1 DR2; Chambers et al. 2016); [11] Dark Energy Survey DR1 (Dark Energy Survey Collaboration et al. 2016); [12] Deep Near Infrared Survey of the Southern Sky third release data (DENIS; Denis 2005); [13] Visible and Infrared Survey Telescope for Astronomy (VISTA; Cross et al. 2012); [14] UKIRT Infrared Deep Sky Survey (UKIDSS; Hewett et al. 2006); [15] 2MASS All-Sky Catalog of Point Sources (2MASS; Skrutskie et al. 2006); [16] Galactic Legacy Infrared Midplane Survey Extraordinaire Source Catalog (GLIMPSE I+II+3D; Spitzer Science 2009); and [17] Wide-field Infrared Survey Explorer AllWISE Data Release (AllWISE; Cutri et al. 2021).

considering all coefficients for a source with one of the highest and another with one of the lowest signal-to-noise ratio.

Of the 12 342 *Gaia* spectra, we obtained 11 447 GJP SEDs with more than four photometric points, the minimum number necessary to be fitted by VOSA, and 12 324 GJP-trunc SEDs. Of them, we obtained a reliable fit ($Vgf_b < 15$) for 11 153 GJP and 11 639 GJP-trunc SEDs, when using either DA or non-DA model spectra. A total of 290 GJP and 678 GJP-trunc SEDs obtained good fits only when using DA model spectra, while no SED obtained a good fit only when using non-DA model spectra. In total, we obtained a good fit for 11 443 GJP and 12 317 GJP-trunc SEDs, almost all the analysed SEDs obtained from *Gaia* spectra. To illustrate, we show some examples of the obtained GJP SEDs and their best-fitting model in Fig. 2 (right-hand panels).

4 WD SPECTRAL CLASSIFICATION

In this section, a set of WD spectral class estimators is built. Most of these estimators were based on the result of the fitting of the SEDs with certain WD atmospheric models as described in the previous section. The performance of these estimators was validated through the spectroscopically confirmed WDs from the MWDD (Dufour et al. 2017).

4.1 Spectral estimators

Following the VOSA procedure, in which each SED was fitted to two models (a DA and a non-DA model), and for which VOSA derived two reduced χ^2-values (χ^2_{DA} and χ^2_{non-DA}, respectively), we built an estimator, *i*, that measures the probability of being a hydrogen-dominated atmosphere (DA) WD, P^i_{DA}, as

$$P^i_{DA} = \frac{1}{2}\left(\frac{\chi^2_{non-DA} - \chi^2_{DA}}{\chi^2_{non-DA} + \chi^2_{DA}} + 1\right). \quad (1)$$

Hence, we classified an object as a DA WD if $P^i_{DA} \geq \eta$, where η is a threshold value, otherwise we considered it as a non-DA. In our analysis, we adopted an initial value of $\eta = 0.5$.

This estimator can be generalized by using any other χ^2-values available in the literature. Hence, up to six estimators were analysed in this work. A description of them is presented as follows, while a summary is listed in Table 3.

4.1.1 The VOSA, VOSA-GJP, and VOSA-GJP-trunc estimators

In Section 3.2, we described the use of VOSA for analysing WD SEDs. For those objects with a reliable fit, i.e. $Vgf_b < 15$, using both DA and non-DA atmospheric model, and by means of equation (1), we built three different estimators. The first one, called VOSA, corresponds to the case that the SEDs were built from public archives within the VO (see Section 3.2). In the case that the SEDs were derived from *Gaia* spectra (see Section 3.3), we defined two extra estimators: If all the coefficients of the WD spectra were taken into account, our estimator is named VOSA-GJP; and in the case that the truncated version of the coefficients was adopted, our estimators is called VOSA-GJP-trunc.

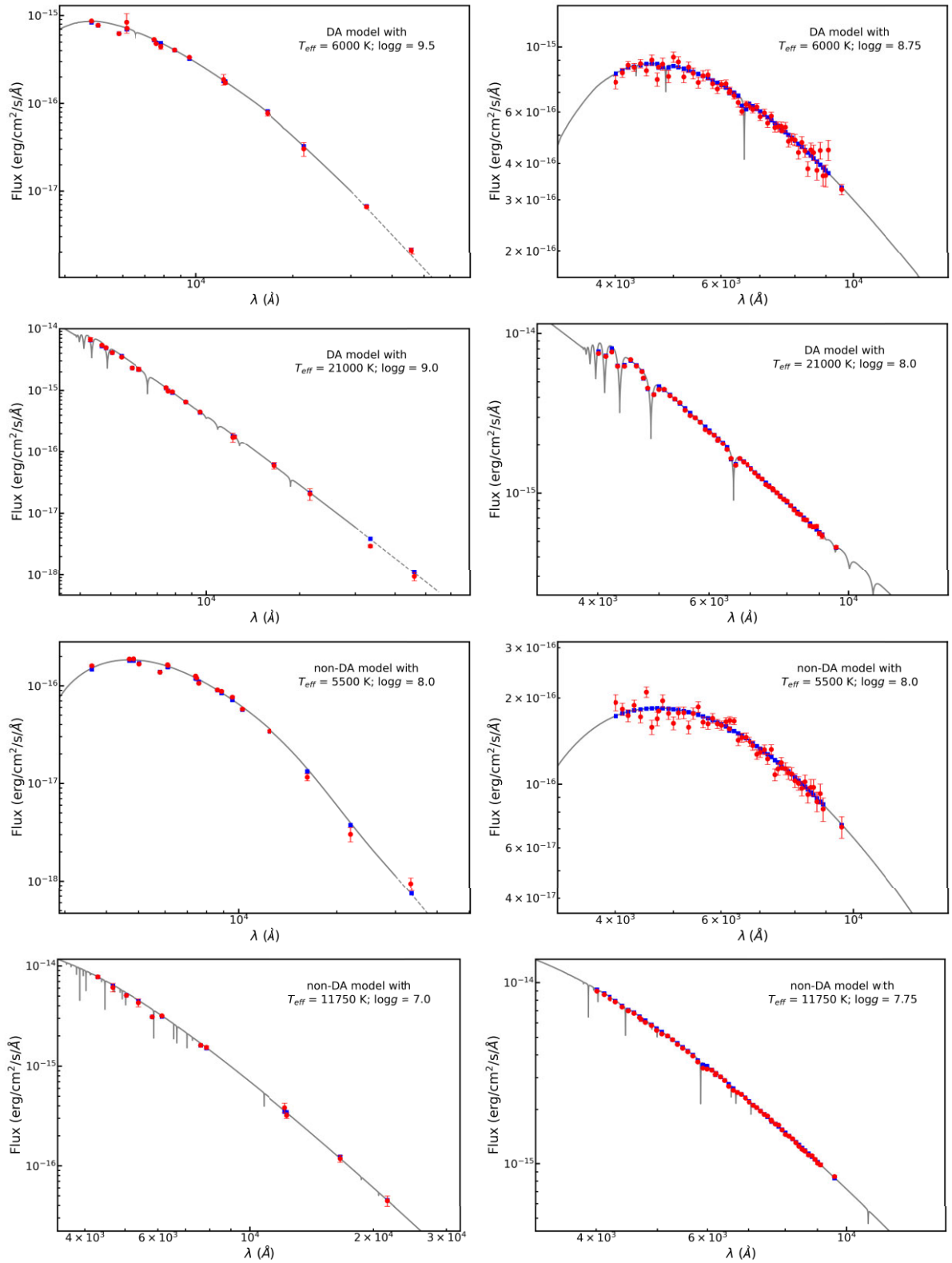

Figure 2. SEDs of four distinct WDs, each row presents an object (from the top to the bottom: *Gaia*-DR3 3750749378584132992, *Gaia*-DR3 3020668542435696512, *Gaia*-DR3 2780434524599787136, and *Gaia*-DR3 5869567658943170048), illustrating DA and non-DA models with different effective temperatures and surface gravities. The red filled circles show the photometry available in VO archives (left-hand panels) and the *Javalambre-Physics of the Accelerating Universe Astrophysical Survey* (J-PAS) photometry built from *Gaia* spectra considering all coefficients (right-hand panels). The best-fitting models are presented as grey solid line, where the blue squares are the synthetic photometry (calculated from the model) in each filter. The dashed line represents the Rayleigh–Jeans law adopted for longer wavelengths, when they are not covered by the models.

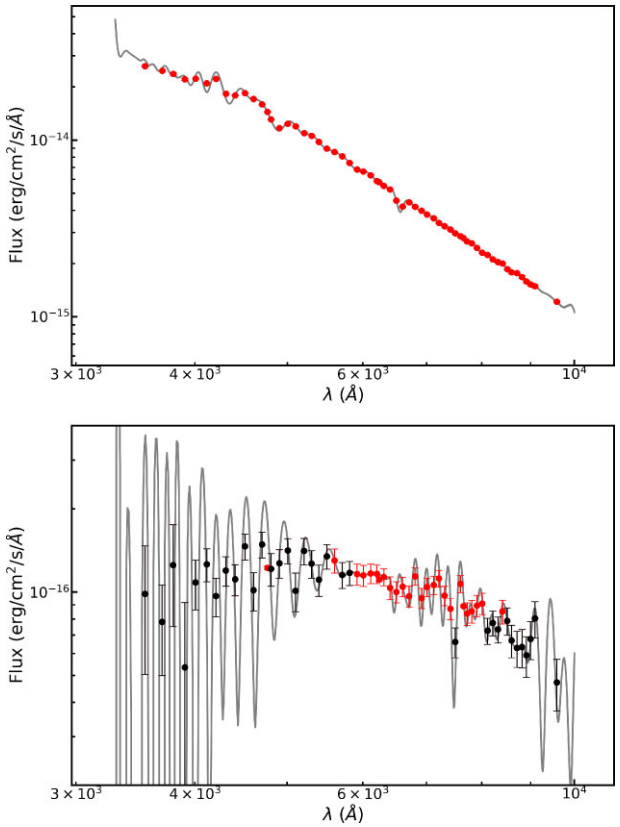

Figure 3. SEDs of two WDs. *Gaia*-DR3 3683519503881169920 (upper panel) has one of the highest signal-to-noise ratio and blue colour ($G_{BP} - G_{RP} \sim -0.32$ mag). On the contrary, *Gaia*-DR3 5174110233491949312 (lower panel) has one of the lowest signal-to-noise ratio and red colour ($G_{BP} - G_{RP} \sim 0.86$ mag). The filled circles show the J-PAS photometry built from *Gaia* spectra considering all coefficients. In red, those photometric points with a relative flux error lower than 10 per cent are shown, and then considered in the model fit, and in black are shown those not considered due to larger errors. The *Gaia* spectra are presented as grey solid lines.

Table 3. Summary of the WD spectral estimator built for this study.

Estimator name	Reference	Atmosphere models	Mean number points per SED
VOSA	This work	Pure hydrogen (Koester 2010) Nearly pure helium H/He= −6 (Koester 2010)	20
VOSA-GJP	This work	idem	56
VOSA-GJP-trunc	This work	idem	56
GF21-I	Gentile Fusillo et al. (2021)	Pure hydrogen (Kowalski et al. 2010; Tremblay, Bergeron & Gianninas 2011) Pure helium (Bergeron et al. 2011)	3
GF21-II	Gentile Fusillo et al. (2021)	Pure hydrogen (Kowalski et al. 2010; Tremblay et al. 2011) Mixed H/He = −5 (Tremblay et al. 2014; McCleery et al. 2020)	3
MON22	Gaia Collaboration (2022a)	*	60

4.1.2 *The GF21-I and GF21-II estimators*

The analysis of the *Gaia* Early Data Release 3 WD population performed by Gentile Fusillo et al. (2021) also provides a fitting of different theoretical atmospheric models to the three *Gaia* passbands: G, G_{RP}, and G_{BP}. Three models were used: one for hydrogen-pure atmospheres of Tremblay et al. (2011) with Ly α opacity of Kowalski et al. (2010), another for pure-helium atmospheres based on Bergeron et al. (2011) models, and the last one for mixed H/He atmospheres with a ratio $\log N(H)/\log N(He) = 10^{-5}$ based on models of Tremblay et al. (2014) and McCleery et al. (2020). All the three models cover the range of effective temperatures and surface gravities of the WDs analysed here (see Gentile Fusillo et al. 2021, and reference therein for further details).

For each atmospheric model – hydrogen-pure, helium-pure, and mixed atmospheres – a χ^2-value, i.e. χ^2_{H-pure}, $\chi^2_{He-pure}$, and χ^2_{mixed}, respectively, was provided in Gentile Fusillo et al. (2021). From the first two χ^2-values, χ^2_{H-pure} and $\chi^2_{He-pure}$ (χ^2_{DA} and χ^2_{non-DA}, respectively), we build our fourth DA probability estimator called GF21-I with the help of equation (1). Similarly, from the first and third χ^2-values, χ^2_{H-pure} and χ^2_{mixed} (χ^2_{DA} and χ^2_{non-DA}, respectively), we generated our fifth estimator named GF21-II.

4.1.3 *The MON22 estimator*

All except one of the estimators analysed in this work follow equation (1). The exception is the sixth estimator used in this work. It is represented by the probability of being a DA estimated by Gaia Collaboration (2022a). In that case, that probability was directly derived from the application of a Random Forest algorithm to the J-PAS synthetic photometry derived from *Gaia*-DR3 spectra.

4.2 Validating sample: the MWDD

MWDD[8] is an open access tool containing spectroscopically classified WDs published in the literature. At the time of writing this article the data base contained 68 364 objects, 3098 of which are within 100 pc from the Sun. From them, we rejected those which are binaries, those with circumstellar disc, and those with tentative spectral classification. This reduced the sample to 2886 sources. We used this data base to construct a validating sample.

It is worth saying here that our WD atmospheric models cover a different range of temperatures, i.e. down to 3000 K for DA and down to 5500 K for non-DA (see Section 3.1). To ensure a proper classification of the *Gaia* sample, we introduced a colour cut. Given that a typical ∼0.6 $M_\odot$ WD with an effective temperature hotter than 5500 K has $G_{BP} - G_{RP} < 0.86$ mag, we restricted our subsequent analysis to objects in this range of *Gaia* colour.

Among the 2886 selected WDs within 100 pc with spectral classification in the MWDD, there are 2400 with $G_{BP} - G_{RP} < 0.86$ mag, that we adopted as a validating sample, represents ∼30 per cent of our 100 pc WD sample in this colour range. In particular, the MWDD validating sample contains 1789 WDs classified as DAs, and 611 WDs of other spectral types DB, DC, DQ, DZ, and similar types, that we assigned to the non-DA group. Thus, the MWDD sample has a ratio of DA to non-DA of 74:26 with a significant fraction of the different spectral types. This fact, together with the aforementioned 30 per cent cross-match with our catalogue, places the MWDD as an excellent validating sample for our spectral estimator tests.

[8] https://www.montrealwhitedwarfdatabase.org/

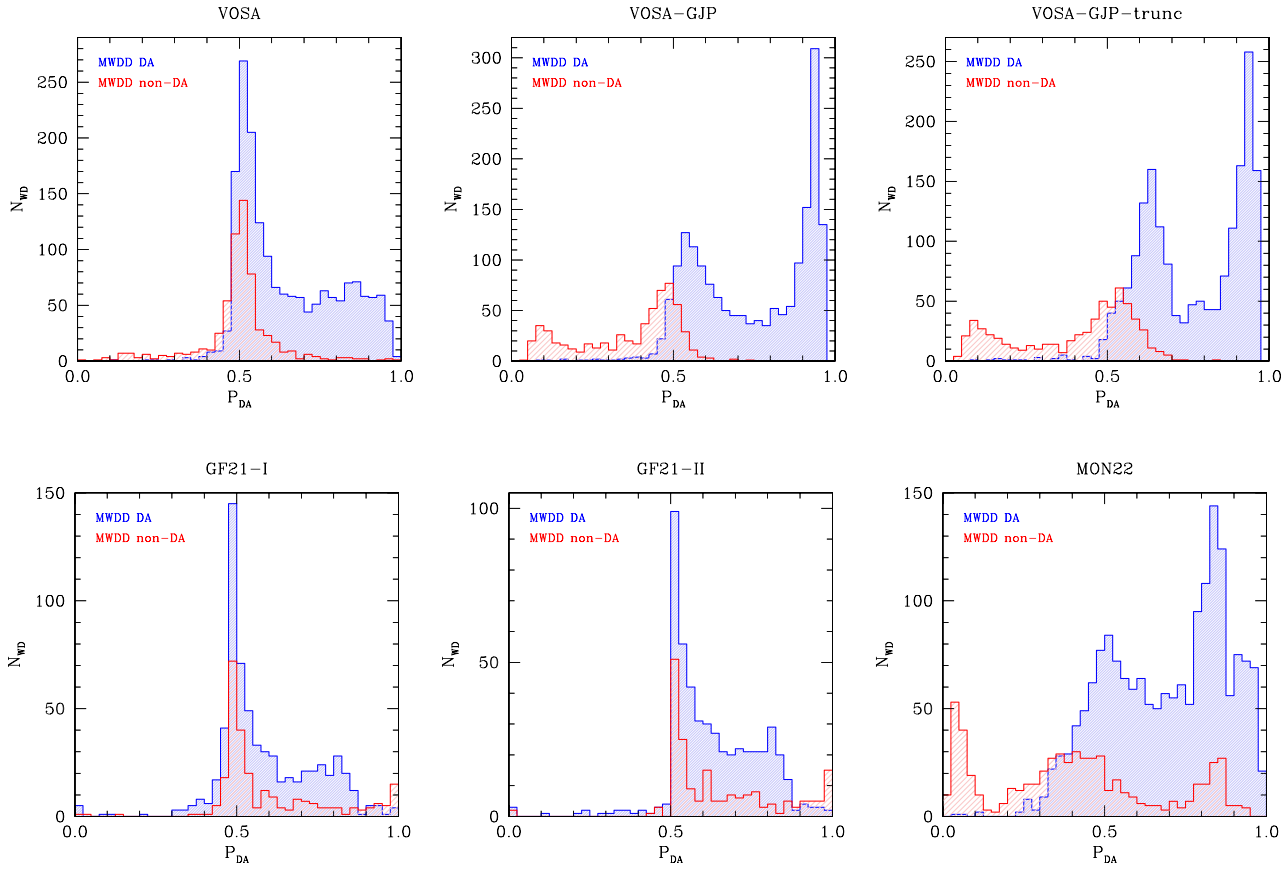

Figure 4. Probability distribution of being DA for the different estimators analysed in this work for the Montreal White Dwarf Database (MWDD) validating sample.

4.3 Results: confusion matrices and scores

In Fig. 4, we show the probability distribution of being DA for the set of estimators under study. The ordinate axis represents the number of WDs, while blue and red histograms correspond to WDs belonging to the DA and non-DA classes, respectively, of the MWDD validating sample. A first glance to the distributions reveals that the pair of estimators VOSA-GJP and VOSA-GJP-trunc (top-middle and top-right panels, respectively) have a similar behaviour, indicating an excellent capability for disentangling DA from non-DA objects. In the case of the VOSA and MON22 estimators (top-left and bottom-right panels, respectively), the general behaviour is also acceptable. However, the fraction of non-DA WDs misclassified as DAs is larger than in the two previous estimators. The last pair of estimators, GF21-I and GF21-II (bottom-left and bottom-middle panels, respectively), seem to have a similar behaviour, correctly identifying practically all DA WDs, but failing in classifying most of the non-DA objects.

The previous analysis can be quantified by means of the confusion matrix, which represents the correlation between the true label object (in our case the MWDD DA or non-DA label; rows) as a function of the predicted label (the DA or non-DA estimator label; columns). The obtained results are shown in Fig. 5, where the displayed values correspond to the total number of objects, the normalized values (in brackets) for each class, and the colour is scaled proportional to the total number of objects considered. The ideal case would correspond to a diagonal matrix with a fraction of DA:non-DA of 74:26, i.e. the fraction presented in the MWDD validating sample. Our estimator VOSA-GJP actually reproduces this ideal case, showing an excellent performance: Only 6 per cent of true-DA WDs are misclassified as non-DA; however, less than 17 per cent of true non-DAs are not properly identified.

In Table 4, we list the accuracy and $F1$ global scores, as well as the sensitivity (also named recall) and the precision for each of the analysed estimators. As previously stated, the estimator VOSA-GJP presents an excellent performance in all the analysed scores. Particularly good are the accuracy and the $F1$ score, 0.91 and 0.94 respectively, as well as the precision of 0.94, reaching these scores the highest values among all the estimators. Regarding the sensitivity, the VOSA-GJP-trunc and GF21-II estimators, with 0.98 and 0.95, respectively, present a slightly better performance than VOSA-GJP, 0.94. However, the better ability of these estimators to retrieve objects of a certain class is worsened by a substantial lower performance regarding the precision with which an object is identified. All in all, the VOSA-GJP can be considered as an excellent estimator for the DA and non-DA WD identification.

Finally, before analysing the physical properties of the identified samples in the next section, a few more checks have been made. As previously stated, for our initial analysis we adopted a threshold value of $\eta = 0.5$. Now, we left η as a free parameter. For the VOSA-GPJ estimator, the value that maximizes the performance is still $\eta \cong 0.5$. For the rest of estimators, slight variations around this value are found. However, in none of the cases the performance of the rest of estimators improved that of the VOSA-GPJ.

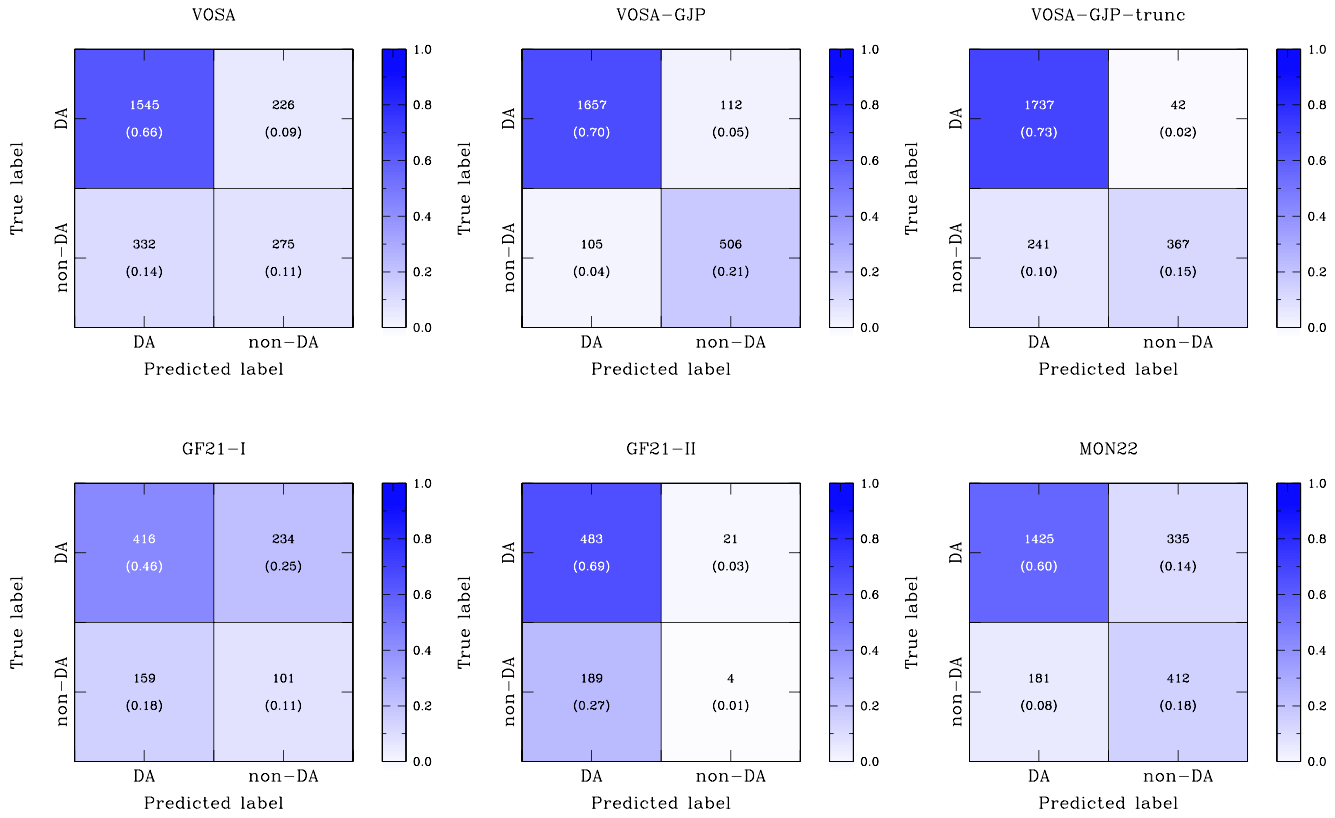

Figure 5. Confusion matrices for the different estimators analysed in this work. Displayed values correspond to the total number of objects, while in brackets the normalized value with respect to the total population. Colour is scaled proportional to the total number of objects considered.

Table 4. Summary of the performance score, sorted from the highest to the lowest accuracy, for the different estimators under study.

Estimator	Accuracy	*F*1 score	Sensitivity	Precision
VOSA-GJP	0.91	0.94	0.94	0.94
VOSA-GJP-trunc	0.88	0.92	0.98	0.88
MON22	0.78	0.85	0.81	0.89
VOSA	0.76	0.85	0.87	0.82
GF21-II	0.70	0.82	0.96	0.72
GF21-I	0.57	0.68	0.64	0.72

5 THE PHYSICAL PROPERTIES OF DA AND NON-DA 100 PC WD POPULATION

In this section, we analyse the physical properties of the 100 pc WD population once classified according to DA or non-DA spectral type by our estimator VOSA-GJP.

We recall here that our analysis is restricted to those WDs with good model fit to the GJP SED and in the *Gaia* colour range $G_{BP} - G_{RP} < 0.86$ mag, which approximately corresponds to a typical ∼0.6 $M_\odot$ WD with an effective temperature just above 5500 K. Thus, we did not expect *BP*-band photometry to be affected by any bias in this colour range, so we use this more common *Gaia* colour in the analysis hereafter.

We show in Fig. 6, the *Gaia* HR diagram for our 100 pc sample, where those objects with an available GJP SED obtained from the non-truncated *Gaia* spectra (see Section 3.3) and a reliable model fit ($Vgf_b < 15$) are marked as blue dots. These objects which represent the 97 per cent of the entire 100 pc WD population. The remaining 7 per cent of objects have either a poor GJP SED fit (green dots) or even no *Gaia* spectrum is available (red dots). As it can be seen, the vast majority of them are faint and red objects. For the colour range considered in the analysis (left to the dashed line), the total number of objects classified is 8150, which represents the 99 per cent of the total population for that range of temperatures. This is up-to-date the most complete spectral type classified sample of WDs.

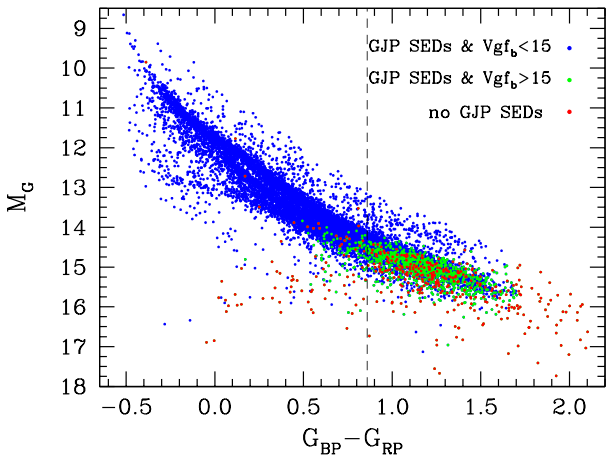

Figure 6. *Gaia* HR diagram of all *Gaia* sources considered in this work. Those with an available GJP SED and a reliable model fit ($Vgf_b < 15$) are marked in blue. These objects in the range of colour $G_{BP} - G_{RP} < 0.86$ (dashed line) are thoroughly analysed in Section 5. Those sources with a bad fit are shown in green, and those with no *Gaia* spectrum available in red. The total percentage of excluded objects represents only 1 per cent in the considered colour range.

5.1 The HR diagram for DA and non-DA WDs

In Fig. 7, we show the *Gaia* HR diagram for our sample of DA (top panel) and non-DA (bottom panel) WDs. For comparative purposes, we have also plotted different spectral types of already classified WDs according to the MWDD. The A, B and Q branches are also pointed (see Gaia Collaboration 2018).

A first glance at Fig. 7 reveals an excellent agreement between the MWDD classified WDs and those classified by our best estimator. This is not surprising since the accuracy of the VOSA-GJP estimator is larger than 90 per cent. Secondly, the loci in the colour–magnitude diagram of the DA and non-DA populations are clearly distinct. The characteristic bifurcation on the HR diagram has been put into manifest since the *Gaia*-DR2. However, the association of each of the two branches, A and B, to a pure-hydrogen or pure-helium atmosphere models, respectively, is a much debated problem (e.g. JE18; Bergeron et al. 2019). In particular, if we assume that the B branch, within $0.1 < G_{BP} - G_{RP} < 0.5$ mag, is formed by WDs with pure-helium atmospheres, this would correspond to average masses larger than the canonical 0.6 $M_{\odot}$ (e.g. Bergeron et al. 2019). Several alternative explanations to avoid this problem have been proposed, such as mixed hydrogen-helium atmospheres, or spectral evolution from hydrogen to helium envelopes, among others (e.g. Bergeron et al. 2019; Ourique et al. 2020). In any case, the characterization of the A and B branches has been limited to the spectroscopically identified WDs in that region, leading to a large fraction of unidentified objects and, consequently, to ignore the real fraction of DA and non-DA in these branches. However, through our analysis, we can confirm that the B branch is mostly but not exclusively formed by non-DA WDs, i.e. 65 per cent of non-DAs and 35 per cent of DAs, while the A branch is practically formed by DA WDs (<6 per cent are non-DAs). Given that the proportion of sources in the A and B branches is 62 and 38 per cent, respectively, this implies that non-DA WDs represent ∼25 per cent of the objects, considering both branches together.

A closer look to the HR diagrams reveals that DA WDs are mostly following the main cooling track (A branch), corresponding to a canonical 0.6 $M_{\odot}$ WD. However, as has been already mentioned, 18 per cent of the objects follow in parallel the main branch along the B branch. This bimodality was pointed out by El-Badry, Rix & Weisz (2018) and it was associated to a flattened in the initial–final mass relationship, which causes an overproduction of 0.8 $M_{\odot}$ WDs. However, other possibilities may contribute to this issue, such as the contribution of WD mergers (e.g. Kilic et al. 2018). Furthermore, a third branch, starting in the Q branch region, is growing in number of objects and joining the main branch at $G_{BP} - G_{RP} \sim 0.8$ mag. As we will analyse in Section 5.2, the net effect is an increase of the average mass as objects are getting cooler. The combined effects of crystallization, ^{22}Ne sedimentation, WD mergers, and probably some other delaying physical cooling processes, may lead to the formation of this extended Q branch (e.g. Cheng, Cummings & Ménard 2019; Tremblay et al. 2019; Kilic et al. 2020; Blouin, Daligault & Saumon 2021; Camisassa et al. 2021).

Regarding the non-DA distribution, apart from the commented fact that they mostly are located in the B branch, we observe a widening of the track for the coolest objects, i.e. $G_{BP} - G_{RP} > 0.6$ mag. In this case, the reverse of the effect than in the DA sample is presented: A decrease in the average mass is expected for cooler non-DA objects. This effect, extended for cooler and less massive objects, was discussed in Bergeron et al. (2019), although no final conclusion was reached. In any case, the true nature of non-DA objects that constitute the B branch, as well as the peculiarities in both diagrams already commented, are beyond the scope of this work.

5.2 Stellar parameter distributions

Relying on updated WD evolutionary models from La Plata group and atmosphere models from Koester (2010), we estimated stellar parameters for the WDs with GJP SED, a reliable model fit (see Section 3.3), and $G_{BP} - G_{RP} < 0.86$ mag. We used different models depending on the spectral classification of the source (see Section 4). For DA WDs, we used the cooling models of Althaus, Miller Bertolami & Córsico (2013) for low-mass helium-core WDs, the models of Camisassa et al. (2016) for average-mass carbon-oxygen-core WDs, and the models of Camisassa et al. (2019) for ultramassive oxygen-neon-core WDs. For non-DA WDs, we employed the hydrogen-deficient cooling models of Camisassa et al. (2017) for average-mass carbon-oxygen-core WDs and Camisassa et al. (2019) for oxygen-neon ultramassive hydrogen-deficient WDs. All these models include realistic initial chemical profiles that are the result of the calculation of the progenitor evolution and consider all the relevant energy sources that govern their evolution. That is, they include neutrino losses, the gravothermal energy released by the ions, the energy released by slow ^{22}Ne sedimentation, and the energy released during the crystallization process, both as latent heat and due to the phase separation (see Camisassa et al. 2022, for details of its implementation). We used the atmosphere models of Koester (2010) to turn these evolutionary models into the magnitudes in the *Gaia* passbands. For DA and non-DA WDs, we employed pure hydrogen and pure helium atmospheres, respectively. Considering the *Gaia* magnitude G and colour $G_{BP} - G_{RP}$ of each of the WDs in our sample, we have interpolated in the theoretical models to obtain their masses and effective temperatures. We excluded all DA WDs with estimated masses below 0.239 $M_{\odot}$ and all non-DA WDs with masses below 0.51 $M_{\odot}$, to avoid extrapolation uncertainties.

In Fig. 8, we show the distribution of WD masses versus effective temperature for our sample of DAs (left-hand panel) and non-DAs (right-hand panel). Also marked are the lines of crystallization onset assuming CO-core for all WDs (solid lines) or adopting ONe-cores for masses above 1.05 $M_{\odot}$ (dotted lines). The crystallization onset was specifically calculated for DA (magenta lines) and non-DA (blue lines) WDs. The distributions obtained reflect most of the peculiarities previously discussed regarding the *Gaia* HR diagram and already analysed in similar diagrams by Bergeron et al. (2019) and Kilic et al. (2020). The bulk of the DAs is formed by objects of ∼0.6 $M_{\odot}$ uniformly distributed for the full range of temperatures. A secondary similar group, with masses around ∼0.8 $M_{\odot}$ but more diffuse can be intuited. Moreover, following the DA crystallization onset line, a group of massive and hot WDs (starting with masses from ∼1.2–1.3 $M_{\odot}$ and ∼30 000 K), whose average mass is decreasing with the temperature is clearly visible. This last trend of stars corresponds to the Q branch and its extension, and they are related to the slow down on the WD cooling rate due to the energy released by crystallization and by the sedimentation of ^{22}Ne (Tremblay et al. 2019; Camisassa et al. 2021). The combined effect of these two later groups of stars for temperatures below 9000 K is an increase on the canonical 0.6 $M_{\odot}$ average mass. Lastly, an increasing number of low-mass stars (due to double-degenerate or unresolved binaries) for lower temperatures is also observable.

Regarding the non-DA distribution of masses and temperatures, we found a lack of ∼0.6 $M_{\odot}$ objects for temperatures between 7000 $< T_{eff} <$ 10 000 K. This effect, as pointed out in Bergeron et al. (2019), can be avoided with the use of other atmospheric models such as mixed hydrogen-helium envelopes, instead of the pure-helium models we used. Likewise, the bulk of WDs that have an average mass of ∼0.6 $M_{\odot}$ at ∼20 000 K, presents a smaller value of ∼0.55

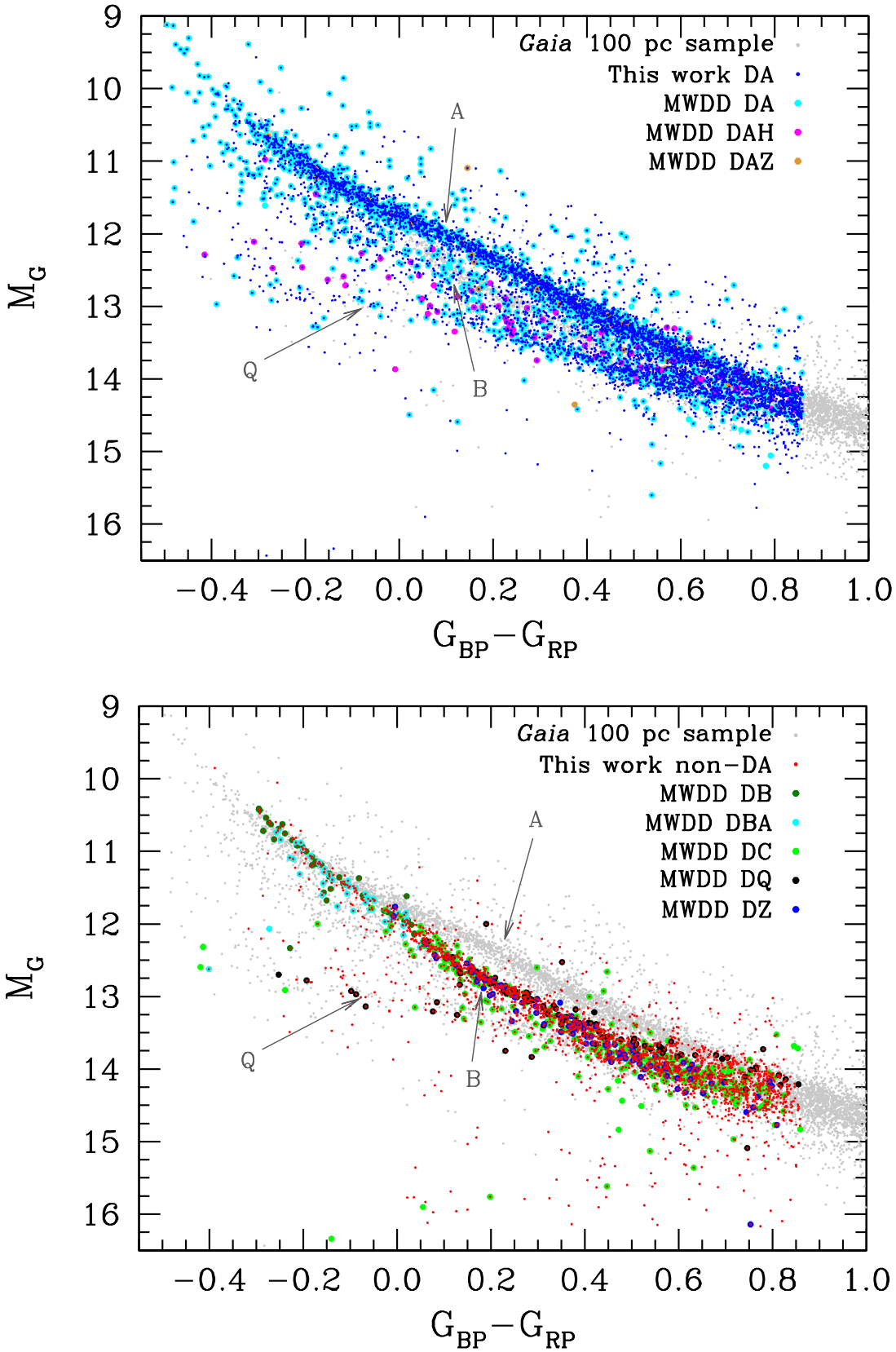

Figure 7. *Gaia* HR diagram for the DA (top panel; blue dots) and non-DA (bottom panel; red dots) WDs classified in this work. Also plotted, for comparative purposes, our entire *Gaia* 100 pc sample (grey dots) and those classified in several spectral types in the MWDD. The A, B, and Q branches are pointed for helping in the discussion.

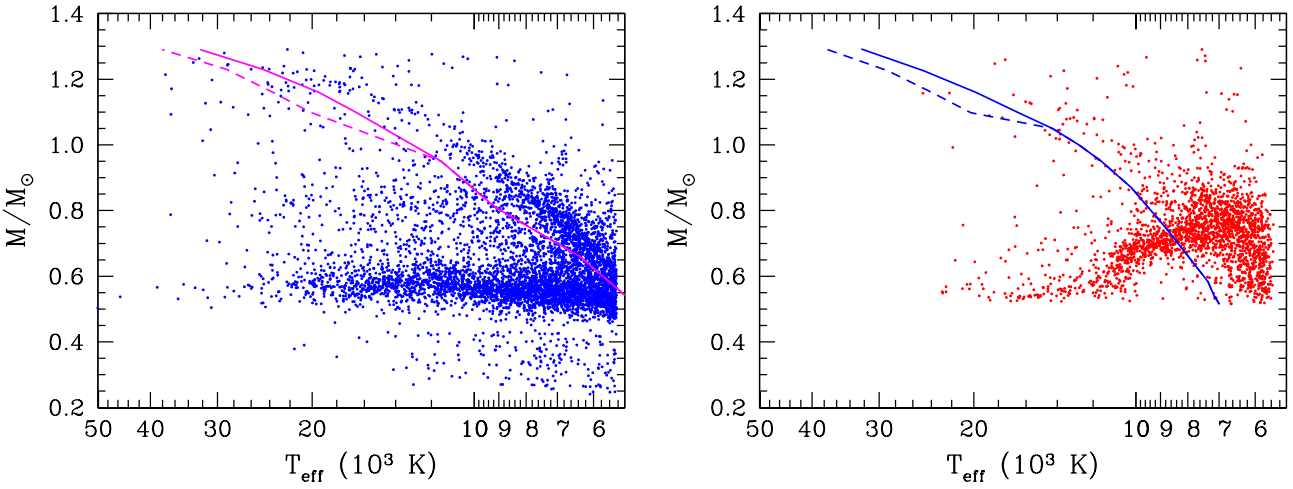

Figure 8. WD masses versus effective temperature for our sample of DA (left-hand panel) and non-DA (right-hand panel). In addition, the crystallization onset assuming CO-core for all WD (solid lines) or ONe-cores for masses above 1.05 $M_\odot$ (dashed lines) are plotted in magenta colour for DAs and in blue for non-DAs.

$M_\odot$ at lower temperatures of ∼6000 K. In any case, it is out of the scope of this study to ascertain the ultimate atmospheric composition of these objects. Independently of this issue, the non-DA distribution also shows a clear increase in the number of massive objects for cooler temperatures.

An individual analysis of the parameters is carried on in Fig. 9, where we show the frequency distribution of effective temperature (left-hand panel) and mass (right-hand panel) for our samples of identified DA (blue histogram) and non-DA (red histogram) WDs. Roughly speaking, the distributions of effective temperatures seem to be similar for DA and non-DA WDs. Although a deficit of non-DA objects is observable for hotter stars, $T_{\rm eff} \gtrsim 12\,000$ K, an excess occurs for cooler temperatures, $T_{\rm eff} \lesssim 9000$ K. We further investigate this issue in the next section.

Regarding the mass distribution, the discrepancies are notorious. The DA distribution shows the canonical peak at $\cong$ 0.58 $M_\odot$, a bump extended up to 0.8 $M_\odot$, and a small fraction of low-mass (non-single origin) WDs. These trends are in agreement with previous reported works (e.g. JE18; Kilic et al. 2020). With regard to the non-DA distribution, a clear bimodality with peaks at ∼0.6 and ∼0.76 $M_\odot$ is present. As stated, this second peak is a consequence of the bifurcation in the HR diagram and the use of pure-helium atmospheres to derive its mass. Otherwise, for instance, in the case of mixed hydrogen-helium atmospheres, this second peak can eventually be removed, or at least reduced. However, if we adopt a flattened initial-to-final mass relationship as in the case of the DA population, a similar peak around 0.8 $M_\odot$ should be expected in the non-DA mass distribution. Under this hypothesis, and assuming the same ratio between the peaks at 0.6 and 0.8 $M_\odot$ as in the DA case (i.e. 80:20 respectively, see right-hand panel of Fig. 9), we would expect that 20 per cent of the non-DA WDs in the B branch to have masses in the range of ∼0.8 $M_\odot$.

Further information can be retrieved when the mass distribution is depicted as a function of the effective temperature. This is done in Fig. 10, where we plot the DA (left-hand panels) and non-DA (right-hand panels) mass distribution for hot ($T_{\rm eff}$ >12 000 K; top panels), medium (7000 < $T_{\rm eff} \leq$ 12 000 K; middle panels), and cool ($T_{\rm eff} \leq$ 7000 K; bottom panels) WDs. These temperature ranges approximately correspond, respectively, to the regions before, during, and after the bifurcation in the *Gaia* HR diagram.

The DA mass distribution for hotter WDs presents the canonical peak at $\cong$ 0.58 $M_\odot$ and an extended tail for massive WDs. However, for $T_{\rm eff} <$ 12 000 K practically no objects more massive than 1.0 $M_\odot$ are found. Two factors should be taken into account. On one hand, as it is seen in Fig. 6, the 1 per cent of sources excluded (red and green dots) in the analysed colour range have larger absolute magnitudes and redder colour. These objects typically correspond to cool massive WDs. On the other hand, as pointed out by Kilic et al. (2020), this absence of more massive stars can be also associated to the delay in the cooling process due to the effect of core crystallization, among others. Moreover, while the main peak remains almost constant regardless of the temperature range, the second one at ∼0.8 $M_\odot$ seems to be more prominent in the middle range of temperatures. Even more, for the coolest WDs an extended tail from 0.6 to 0.8 $M_\odot$ appears. This feature is indicative that, even assuming the bimodality is caused by the flattened of the initial–final mass relationship, an additional process such as the contribution of the merger WD population needs to be added to this scenario. Some of these features on the mass–temperature distribution have been partially guessed in previous works (e.g. Kepler et al. 2007; Tremblay et al. 2010, 2016; Rebassa-Mansergas et al. 2015a, b). However, it was not until the arrival of the data provided by the *Gaia*-DR3 that we had a full picture of the mass–temperature distribution of the WD population.

In the case of the non-DA mass distribution, the dependence with the effective temperature is stronger than in the previous case. While the hottest non-DA WDs peak at $\cong$ 0.58 $M_\odot$ with an extended tail up to massive WDs, the non-DA mass distribution for medium temperatures peaks at $\cong$ 0.75 $M_\odot$. We recall that this range of effective temperatures corresponds to the bifurcation and that the increase of the average mass is likely a consequence of the use of pure-helium atmospheres for WDs in the B branch. In the case of the coolest non-DA WDs, an extended fraction of low mass (<0.6 $M_\odot$) WDs appears. Nevertheless, all these features on the non-DA mass distribution should be taken with caution, given that we are assuming pure-helium atmospheres for all non-DA objects, and that a combination of different atmospheres such a mixed, carbon-contaminated, etc., is expected to be present in the observed sample.

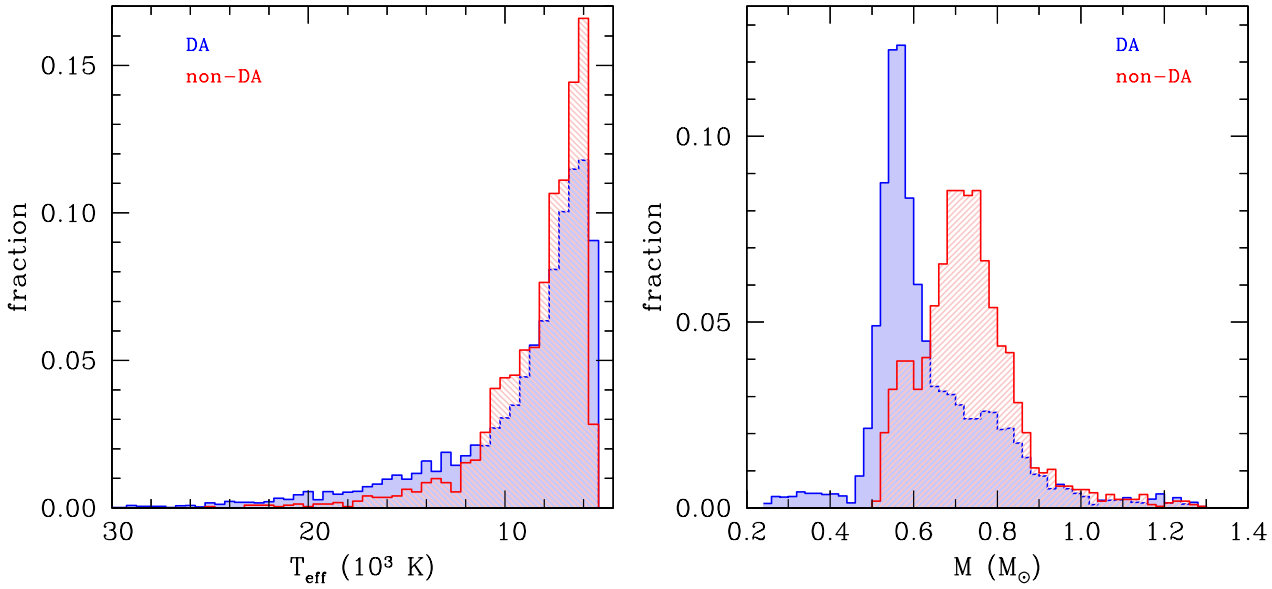

Figure 9. Distributions of effective temperature (left-hand panel) and mass (right-hand panel) for our sample of identified DA (blue histograms) and non-DA (red histogram). See text for details.

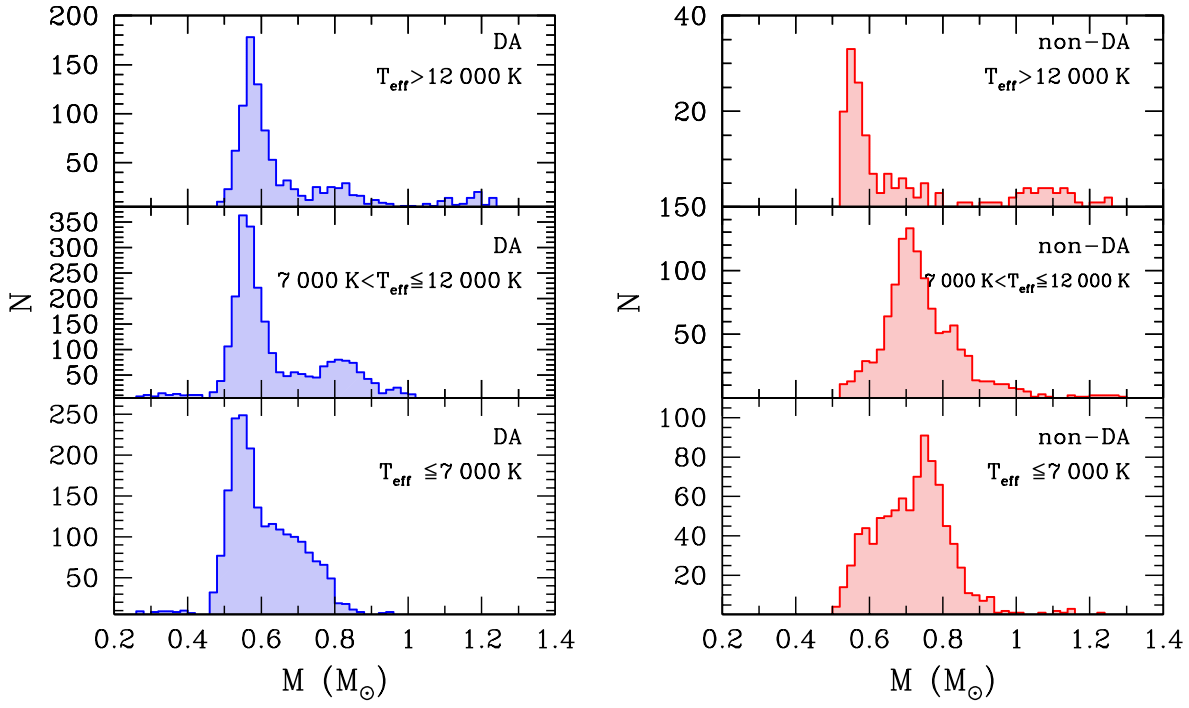

Figure 10. Distribution of mass for our sample of identified DA (left-hand panels) and non-DA (right-hand panels) in different range of temperatures.

5.3 The ratio of DA to non-DA WDs

The ratio of DA to non-DA WDs as a function of the effective temperature, also commonly referred to as the spectral evolution, is a capital tool for understanding the evolutionary processes in WD atmospheres (e.g. Cunningham et al. 2020; Ourique et al. 2020, and references therein). Due to the diversity of selection effects, one of the major problems that previous studies had to face when building a detailed spectral evolution function was the incompleteness of the analysed samples. However, based on the robustness of our estimator built from *Gaia* spectra, we could analyse with a highly degree of completeness our statistically significant 100 pc WD sample. That is, we can consider it as a volume limited sample, thus avoiding the need of any assumption on correcting factors. Furthermore, our analysis allowed to reconstruct the spectral evolution for a wide range of effective temperatures, from 25 000 to 5500 K.

In Fig. 11, we show the ratio of non-DA WDs with respect to the total number of objects as a function of effective temperature (black line). We recall that our classification was done for the *Gaia* colour range $G_{BP} - G_{RP} < 0.86$ mag, corresponding to $T_{eff} > 5500$ K and, in order to avoid the effect of unresolved binaries, we selected

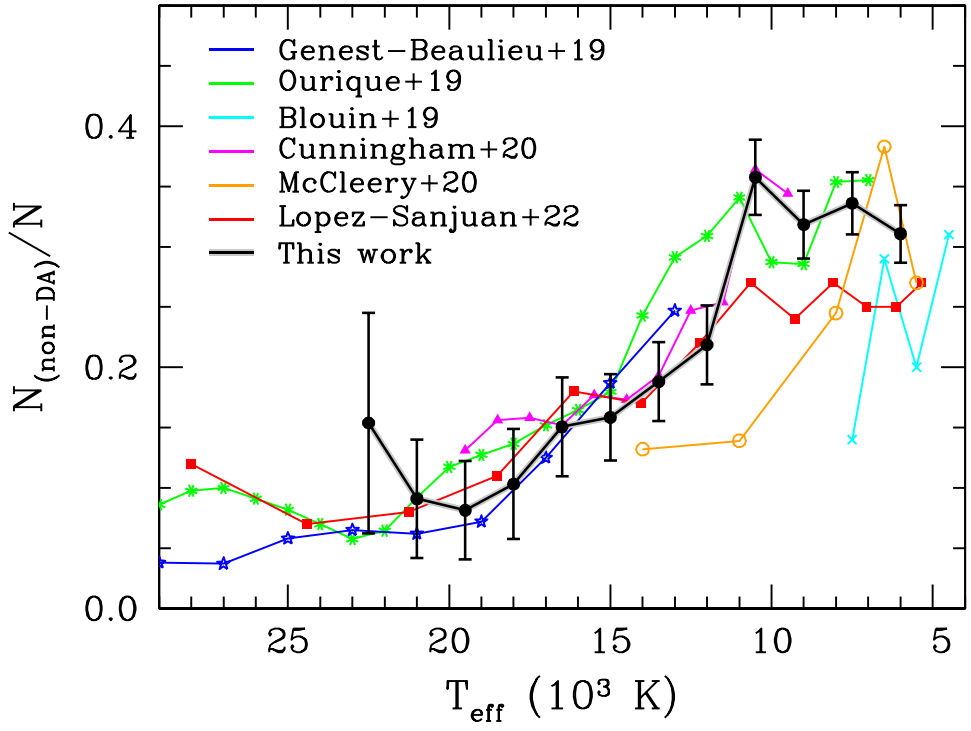

Figure 11. *Gaia* ratio of DA versus non-DA for our sample of identified WDs (black points and lines). Objects with $M_{\rm WD} < 0.51$ M$_\odot$ has been disregarded to avoid contamination from unresolved binaries. For comparative purposes, we also show spectral evolution distributions from other works.

objects only with $M_{\rm WD} > 0.51$ M$_\odot$. Error bars were estimated as $\sigma_f = \sqrt{f \times (1-f)/N}$, where f is the fraction of non-DA to the total number of objects, N, and weighting the contribution of each object according to the probability of being DA. For comparative purposes, we also show some other distributions recently published in the literature.

The first characteristic of our spectral evolution function is the general smooth behaviour, a direct consequence of the high degree of completeness of our sample. Secondly, error bars are larger for hotter temperatures, given that our 100 pc volume-limited sample is relatively small in comparison to magnitude-limited samples, and thus, the scarcity in hot objects. However, the higher resolution of our distribution for cooler temperatures is evident. Analysing the particular details of our distribution, we discern some of the characteristics already presented in previous works. For instance, in the range of temperatures between ∼23 000 and ∼13 000 K, our spectral distribution is nearly constant with an average ratio of ∼13 per cent and a slight growth up to 13 000 K. This behaviour is compatible with most of the distributions: Ourique et al. (2020), López-Sanjuan et al. (2022), Cunningham et al. (2020), and Genest-Beaulieu & Bergeron (2019). At that point, there is an abrupt increase that reaches its maximum fraction, $f \cong 36$ per cent at $T_{\rm eff} \sim 10\,500$ K, which corresponds to the bifurcation zone in the *Gaia* HR diagram. A similar high ratio is also found in Cunningham et al. (2020) and Ourique et al. (2020). In particular, our distribution perfectly resembles that of Cunningham et al. (2020). For cooler temperatures, the fraction decreases down to $f \cong 0.31$ for the coolest bin ($T_{\rm eff} \sim$ 5500 K). A similar trend is also found by McCleery et al. (2020). On the contrary, we have found no evidences of an increase ratio of non-DA to DA between $6250 \leq T_{\rm eff} \leq 7500$ K due to convective mixing, as predicted by Blouin et al. (2019). However, as it is evident from the discrepancies among the distributions, any conclusion in the cooler range of temperatures should be taken with caution, as larger photometric errors and selection biases dominate in this region.

6 CONCLUSIONS

An update of our 100 pc WD sample (JE18) was performed, taking advantage of the new photometric and astrometric data together with the low-resolution spectra provided by the *Gaia*-DR3. A total of 12 718 WDs configure our new catalogue, from which 12 342 have *Gaia* spectra. This constitutes the largest nearly complete volume-limited WD sample available to date.

The use of automated algorithms for fitting and analysing SEDs, provided by the SVO, and in particular VOSA, allowed us to extract the maximum information from the SED of the WDs in our sample. In this sense, we built an estimator of the probability of being DA from the fitting of hydrogen-rich and nearly helium-pure atmosphere models to the synthetic J-PAS photometry derived from the *Gaia* spectra, when all the coefficients are taken into account. The statistical analysis carried out when comparing this estimator with two others also built in this work and others available from the literature, revealed its superior performance. The validating test by using the spectral classification from the MWDD showed an accuracy larger than 90 per cent, together with a precision and a sensitivity of 94 per cent.

The excellent results in the identification of DA and non-DA WDs led us to apply this estimator to the entire population with an effective temperature above 5500 K. A total of 8150 objects (representing the 99 per cent of objects of our catalogue in that range of temperatures) have been spectrally classified in these two main groups. This classification has allowed precisely determining the proportion of DA and non-DA objects in the different regions of the *Gaia* HR diagram.

Our results showed that the A branch in the region $0.1 < G_{BP} - G_{RP} < 0.5$ mag is practically formed by DA stars (94 per cent); however, the B branch, although mainly constituted by non-DA WDs (65 per cent), contains a significant fraction of DA WDs (35 per cent). These results imply, on one hand, the confirmation of a bimodality in the DA mass distribution [some hypotheses have outlined such a stepper initial-to-final mass relation or the contribution of WD mergers (e.g. El-Badry et al. 2018; Kilic et al. 2018)]; on the other hand, the practically non-existence of non-DA WDs in the A branch is indicative that helium-pure atmospheres suffer from some mixing process, leading to mixed envelopes for temperatures below 12 000 K. However, we cannot ensure that all non-DA WDs in the B branch present a mixed atmosphere. Assuming the bimodality argument of the DA population caused by the flattened initial-to-final mass relation, in the case of non-DA WDs, this scenario would imply that 20 per cent of non-DAs are genuine $\sim$0.8 $M_\odot$ WDs. In any case, the ultimate characterization of these atmospheres is beyond the scope of this work.

Our analysis also allowed us to derive stellar parameters by means of photometric interpolation in updated cooling sequences from La Plata models with hydrogen-pure or helium-pure atmosphere models. This way we built, e.g. the mass distribution for DA and non-DA stars. Our results showed a bimodality in the DA mass distribution, as previously commented and already reported in the literature, with a main peak at $\sim$0.58 $M_\odot$ and a secondary one at $\sim$0.8 $M_\odot$. An extended tail for WDs more massive than 0.8 $M_\odot$ is also observed for $T_{\rm eff} > 12\,000$ K that disappears for lower temperatures due to a combination of crystallization and other physical process along with incompleteness bias effects. It was also noticed that for temperatures below 7000 K the second peak fades. A possible cause is that for this low range of temperatures, crystallization starts to happen for WD less massive than 0.8 $M_\odot$, smoothing out the mass distribution between the two peaks. Regarding the non-DA mass distribution, although a preliminary guess was done by using helium-pure models, some conclusions may be drawn. A clear peak at $\sim$0.58 $M_\odot$ mainly formed by genuine DB stars is present for temperatures above 12 000 K. This peak is moved to $\sim$0.72 $M_\odot$ at lower temperatures as a consequence of fitting the B branch with helium pure atmospheric models. However, for the lowest temperatures, the initial peak at even slightly less massive value $\sim$0.56 $M_\odot$ reappears. These facts indicate that individual spectral identification of WDs atmosphere – i.e. DB, DBA, DQ, DZ, etc. – is required in other to properly determine the non-DA mass distribution.

Finally, our analysis also allowed us to derive a precise ratio of non-DA to DA WDs as a function of the effective temperature. Our spectral evolution distribution revealed a $\sim$13 per cent non-DA fraction nearly constant smoothly increasing up to effective temperatures of $\sim$13 000 K, in excellent agreement with most of the recent published distributions. For lower temperatures, a marked growth was found reaching its maximum fraction of 36 per cent at $\sim$10 500 K, in perfect agreement with the spectral evolution function of Cunningham et al. (2020) and also compatible with that from Ourique et al. (2020). Although for lower temperatures our result should be taken with caution, we found a decrease in the ratio of non-DA leading to a fraction of $\sim$31 per cent at $\sim$5500 K.

In summary, the conjunction of accurate WD models, the excellent observational data base provided by *Gaia*, and the capabilities of automated tools such as the VO SED Analyzer, allowed us to achieve the up-to-date largest spectral characterization of the volume-limited WD population in our solar neighbourhood, open thus the door to future studies, such as its luminosity function or the star history of this region of the Galaxy.

ACKNOWLEDGEMENTS

We are greatly indebted to Detlev Koester for providing us with his white dwarf model atmosphere spectra. ST acknowledges fruitful discussion and data provided by Carlos López-Sanjuan. We also thank to the referee Dr Jay Holberg for his valuable comments.

FJE acknowledges financial support from the Servicio Püblico de Empleo Estatal, Spain. PC acknowledges financial support from the Government of Comunidad Autönoma de Madrid (Spain) via postdoctoral grant 'Atracciön de Talento Investigador' 2019-T2/TIC-14760. ST and ARM acknowledge support from MINECO under the PID2020-117252GB-I00 grant. ARM acknowledges support from Grant RYC-2016-20254 funded by MCIN/AEI/10.13039/501100011033 and by ESF Investing in your future. RMO is funded by INTA through grant PRE-OBSERVATORIO. MEC acknowledges support from NASA grants (HGC) 80NSSC17K0008 and (LWS) 80NSSC20K0193 and the University of Colorado Boulder.

This work has made use of data from the European Space Agency (ESA) mission *Gaia* (https://www.cosmos.esa.int/gaia), processed by the *Gaia* Data Processing and Analysis Consortium (DPAC, https://www.cosmos.esa.int/web/gaia/dpac/consortium). Funding for the DPAC has been provided by national institutions, in particular the institutions participating in the *Gaia* Multilateral Agreement. This work has made use of the Python package *GAIAXPY*, developed and maintained by members of the *Gaia* Data Processing and Analysis Consortium (DPAC) and in particular, Coordination Unit 5 (CU5), and the Data Processing Centre located at the Institute of Astronomy, Cambridge, UK (DPCI). This publication makes use of VOSA, developed under the Spanish Virtual Observatory (https://svo.cab.inta-csic.es) project funded by MCIN/AEI/10.13039/501100011033/ through grant PID2020-112949GB-I00. We extensively made use of TOPCAT (Taylor 2005). This research has made use of the VizieR catalogue access tool, CDS, Strasbourg, France. We acknowledge use of the ADS bibliographic services.

7 DATA AVAILABILITY

The '100 pc white dwarf *Gaia*-DR3 catalogue' is available online as supplementary material hosted by the journal and at the 'SVO archive of *Gaia* white dwarfs'[9] (see Appendix A) at the Spanish Virtual Observatory portal.[10]

REFERENCES

Alam S. et al., 2015, ApJS, 219, 12
Althaus L. G., Córsico A. H., Isern J., García-Berro E., 2010, A&AR, 18, 471
Althaus L. G., Miller Bertolami M. M., Córsico A. H., 2013, A&A, 557, A19
Barentsen G. et al., 2014, MNRAS, 444, 3230
Bayo A., Rodrigo C., Barrado y Navascués D., Solano E., Gutiérrez R., Morales-Calderón M., Allard F., 2008, A&A, 492, 277
Benitez N. et al., 2014, preprint (arXiv:1403.5237)
Bergeron P. et al., 2011, ApJ, 737, 28
Bergeron P., Dufour P., Fontaine G., Coutu S., Blouin S., Genest-Beaulieu C., Bédard A., Rolland B., 2019, ApJ, 876, 67
Bianchi L., Shiao B., Thilker D., 2017, ApJS, 230, 24
Blouin S., Dufour P., Thibeault C., Allard N. F., 2019, ApJ, 878, 63

[9] http://svo2.cab.inta-csic.es/vocats/v2/wdw
[10] https://svo.cab.inta-csic.es/docs/index.php?pagename=Archives

Blouin S., Daligault J., Saumon D., 2021, ApJ, 911, L5
Bonoli S. et al., 2021, A&A, 653, A31
Camisassa M. E., Althaus L. G., Córsico A. H., Vinyoles N., Serenelli A. M., Isern J., Miller Bertolami M. M., García–Berro E., 2016, ApJ, 823, 158
Camisassa M. E., Althaus L. G., Rohrmann R. D., García-Berro E., Torres S., Córsico A. H., Wachlin F. C., 2017, ApJ, 839, 11
Camisassa M. E. et al., 2019, A&A, 625, A87
Camisassa M. E., Althaus L. G., Torres S., Córsico A. H., Rebassa-Mansergas A., Tremblay P.-E., Cheng S., Raddi R., 2021, A&A, 649, L7
Camisassa M. E., Althaus L. G., Koester D., Torres S., Gil-Pons P., Córsico A. H., 2022, MNRAS, 511, 5198
Cenarro A. J. et al., 2019, A&A, 622, A176
Chambers K. C. et al., 2016, preprint (arXiv:1612.05560)
Cheng S., Cummings J. D., Ménard B., 2019, ApJ, 886, 100
Cross N. J. G. et al., 2012, A&A, 548, A119
Cunningham T., Tremblay P.-E., Gentile Fusillo N. P., Hollands M., Cukanovaite E., 2020, MNRAS, 492, 3540
Cutri R. M. et al., 2021, VizieR Online Data Catalog. p. II/328
Dark Energy Survey Collaboration et al., 2016, MNRAS, 460, 1270
De Angeli F. et al., 2022, preprint (arXiv:2206.06143)
Denis C., 2005, VizieR Online Data Catalog. p. B/denis
Drew J. E. et al., 2016, VizieR Online Data Catalog. p. II/341
Dufour P., Blouin S., Coutu S., Fortin-Archambault M., Thibeault C., Bergeron P., Fontaine G., 2017, in Tremblay P. E., Gaensicke B., Marsh T., eds, ASP Conf. Ser. Vol. 509, 20th European White Dwarf Workshop. Astron. Soc. Pac., San Francisco, p. 3
El-Badry K., Rix H.-W., Weisz D. R., 2018, ApJ, 860, L17
Fabricius C. et al., 2021, A&A, 649, A5
Fontaine G., Brassard P., Bergeron P., 2001, PASP, 113, 409
Gaia Collaboration, 2016, A&A, 595, A1
Gaia Collaboration, 2018, A&A, 616, A10
Gaia Collaboration, 2022a, preprint (arXiv:2206.06215)
Gaia Collaboration, 2022b, preprint (arXiv:2208.00211)
García-Berro E., Oswalt T. D., 2016, New Astron. Rev., 72, 1
Genest-Beaulieu C., Bergeron P., 2019, ApJ, 882, 106
Gentile Fusillo N. P. et al., 2021, MNRAS, 508, 3877
Henden A. A., Levine S., Terrell D., Welch D. L., 2015, American Astronomical Society Meeting Abstracts, 336.16
Hewett P. C., Warren S. J., Leggett S. K., Hodgkin S. T., 2006, MNRAS, 367, 454
Holberg J. B., Oswalt T. D., Sion E. M., Barstow M. A., Burleigh M. R., 2013, MNRAS, 435, 2077
Hollands M. A., Tremblay P. E., Gänsicke B. T., Gentile-Fusillo N. P., Toonen S., 2018, MNRAS, 480, 3942
Høg E. et al., 2000, A&A, 355, L27
Isern J., Torres S., Rebassa-Mansergas A., 2022, Frontiers Astron. Space Sci., 9, 6
Jiménez-Esteban F. M., Torres S., Rebassa-Mansergas A., Skorobogatov G., Solano E., Cantero C., Rodrigo C., 2018, MNRAS, 480, 4505
Kepler S. O., Kleinman S. J., Nitta A., Koester D., Castanheira B. G., Giovannini O., Costa A. F. M., Althaus L., 2007, MNRAS, 375, 1315
Kilic M., Hambly N. C., Bergeron P., Genest-Beaulieu C., Rowell N., 2018, MNRAS, 479, L113
Kilic M., Bergeron P., Kosakowski A., Brown W. R., Agüeros M. A., Blouin S., 2020, ApJ, 898, 84
Koester D., 2010, Mem. Soc. Astron. Ital., 81, 921
Kowalski A. F., Hawley S. L., Holtzman J. A., Wisniewski J. P., Hilton E. J., 2010, ApJ, 714, L98
Lindegren L. et al., 2021, A&A, 649, A2
López-Sanjuan C. et al., 2022, A&A, 658, A79
Lutz T. E., Kelker D. H., 1973, PASP, 85, 573
McCleery J. et al., 2020, MNRAS, 499, 1890
Marín-Franch A. et al., 2012, in Navarro R., Cunningham C. R., Prieto E., eds, Proc. SPIE Conf. Ser. Vol. 8450, Modern Technologies in Space- and Ground-based Telescopes and Instrumentation II. SPIE, Bellingham, p. 84503S
Ourique G., Kepler S. O., Romero A. D., Klippel T. S., Koester D., 2020, MNRAS, 492, 5003
Page M. J. et al., 2012, MNRAS, 426, 903
Rebassa-Mansergas A. et al., 2015a, MNRAS, 450, 743
Rebassa-Mansergas A., Rybicka M., Liu X. W., Han Z., García-Berro E., 2015b, MNRAS, 452, 1637
Riello M. et al., 2021, A&A, 649, A3
Rodrigo C., Solano E., 2020, in XIV.0 Scientific Meeting (Virtual) of the Spanish Astronomical Society. p. 182
Rodrigo C., Solano E., Bayo A., 2012, SVO Filter Profile Service Version 1.0, IVOA Working Draft
Sion E. M., Greenstein J. L., Landstreet J. D., Liebert J., Shipman H. L., Wegner G. A., 1983, ApJ, 269, 253
Skrutskie M. F. et al., 2006, AJ, 131, 1163
Spitzer Science C., 2009, VizieR Online Data Catalog. p. II/293
Tassoul M., Fontaine G., Winget D. E., 1990, ApJS, 72, 335
Taylor M. B., 2005, in Shopbell P., Britton M., Ebert R., eds, ASP Conf. Ser. Vol. 347, Astronomical Data Analysis Software and Systems XIV. Astron. Soc. Pac., San Francisco, p. 29
Torres S., Canals P., Jiménez-Esteban F. M., Rebassa-Mansergas A., Solano E., 2022, MNRAS, 511, 5462
Tremblay P. E., Bergeron P., 2009, ApJ, 696, 1755
Tremblay P. E., Bergeron P., Kalirai J. S., Gianninas A., 2010, ApJ, 712, 1345
Tremblay P. E., Bergeron P., Gianninas A., 2011, ApJ, 730, 128
Tremblay P. E., Kalirai J. S., Soderblom D. R., Cignoni M., Cummings J., 2014, ApJ, 791, 92
Tremblay P. E., Cummings J., Kalirai J. S., Gänsicke B. T., Gentile-Fusillo N., Raddi R., 2016, MNRAS, 461, 2100
Tremblay P.-E. et al., 2019, Nature, 565, 202
York D. G. et al., 2000, AJ, 120, 1579
Zhao G., Zhao Y.-H., Chu Y.-Q., Jing Y.-P., Deng L.-C., 2012, Res. Astron. Astrophys., 12, 723

SUPPORTING INFORMATION

Supplementary data are available at *MNRAS* online.

suppl_data

Please note: Oxford University Press is not responsible for the content or functionality of any supporting materials supplied by the authors. Any queries (other than missing material) should be directed to the corresponding author for the article.

APPENDIX A: ONLINE CATALOGUE SERVICE

In order to help the astronomical community on using our catalogue of WDs, we developed a wed archive system that can be accessed from a webpage[11] or through a VO ConeSearch.[12]

The archive system implements a very simple search interface that permits queries by coordinates and radius as well as by other parameters of interest. The user can also select the maximum number of sources (with values from 10 to unlimited) and the number of columns to return (minimum, default, or maximum verbosity).

The result of the query is a HTML table with all the sources found in the archive fulfilling the search criteria. The result can also be downloaded as a VOTable or a CSV file. Detailed information on the output fields can be obtained placing the mouse over the question mark ('?') located close to the name of the column. The archive also

[11] http://svo2.cab.inta-csic.es/vocats/v2/wdw/

[12] For example, http://svo2.cab.inta-csic.es/vocats/v2/wdw/cs.php?RA=301.708&DEC=-67.482&SR=0.1&VERB=2.

implements the Simple Application Messaging Protocol[13] (SAMP) VO protocol. SAMP allows VO applications to communicate with each other in a seamless and transparent manner for the user. This way, the results of a query can be easily transferred to other VO applications, such as, e.g. TOPCAT.

[13]http://www.ivoa.net/documents/SAMP/

This paper has been typeset from a TEX/LATEX file prepared by the author.